

Crystalline Phase Reduction of Cuprous Oxide (Cu₂O) Nanoparticles Accompanied by a Morphology Change during Ethanol-Assisted Spray Pyrolysis

Dudi Adi Firmansyah,[†] Taeil Kim,[†] Songkil Kim,[†] Kyle Sullivan,[‡] Michael R. Zachariah,[‡] and Donggeun Lee^{*†}

[†]School of Mechanical Engineering, Pusan Clean Coal Center, Pusan National University, Busan 609-735, South Korea, and [‡]Department of Mechanical Engineering and Department of Chemistry and Biochemistry, University of Maryland, Maryland 20742

Received January 11, 2009. Revised Manuscript Received March 27, 2009

Metallic copper nanoparticles are produced by spray pyrolysis of copper nitrates with an addition of ethanol as cosolvent at 600 °C. Depending on the synthesis temperature, two interesting reaction pathways are found: below 525 °C, ~10% of hollow Cu₂O parent particles are oxidized to CuO and then reduced to Cu, but at higher temperature, the remaining Cu₂O takes a direct path to Cu, accompanied by a morphology change. These interesting reaction regimes are discussed in the aspects of phase-transformation kinetics, gas-phase and solid-phase thermodynamics, force balance, and their possible influences on structural instability. Experimental observations are fairly consistent with the predictions by the present models.

1. Introduction

Copper nanoparticles are of considerable interest because of their high potential in various fields such as electrode materials,¹ catalysts,² electronics,³ and gas sensors.⁴ Copper nanoparticles have been prepared by several methods ranging from thermal reduction,⁵ sonochemical method,⁵ sol-gel reaction,⁶ to gas-phase process.^{7,8} Compared to the wet-phase sol-gel based method and the thermal reduction, both of which require inherent multistep processes, gas-phase methods are capable of continuous production of nanoparticles with a single step. Therefore, many modifications of the gas-phase method including inert gas condensation,⁹ sputtering,¹⁰ microwave synthesis,¹¹ and spray pyrolysis¹² have been developed for large-scale industrial production of nanoparticles.⁸ Among those, the spray pyrolysis has several advantages over the others in the aspects of simple operation,⁸ good purity,¹³ excellent control of chemical dispersion,¹⁴ stoichiometry in mixed oxide systems,¹⁵ and continuous operation.¹⁶

Since spray pyrolysis of oxygen-containing metal salts typically proceeds at elevated temperatures, this method very often produces metal oxide^{17–23} including CuO^{17,19,20} in air or even in inert gas. For this reason, a generation of Cu nanoparticles^{17,19,20} using spray pyrolysis itself is essentially challenging. Addition of a reducing gas such as H₂ or CO to the carrier gas is known to facilitate the reduction of CuO to Cu.¹⁹ However, in this case, the concentration of H₂ required for the reduction of CuO might be greater than the flammability criteria of H₂ in air. To avoid the potential safety problem, Kim et al.¹⁷ proposed a simple idea of the cogeneration of H₂ in the course of spray pyrolysis rather than the injection of H₂ prior to the reaction. They demonstrated the generation of phase-pure copper through spray pyrolysis of copper nitrate and copper acetate precursors using ethanol as the cosolvent over the temperature range 450–1000 °C. They used the fact that ethanol decomposes primarily to a strong reducing atmosphere H₂ during spray pyrolysis. Though they took a big step toward the safe continuous production of controlled Cu nanoparticles, their successive study²⁰ was focused mainly on ethanol decomposition and a thermodynamic discussion in the absence of hydrogen. An investigation that focuses on the condensed phase is currently warranted.

In this study, we produce copper nanoparticles via spray pyrolysis at lower temperatures of 450–600 °C (Figure 1). The influences of ethanol concentration and reaction temperature on morphology, particle size, and crystalline phase are investigated in detail. The simultaneous phase transformation of copper oxide is explored from a kinetic point of view at a variety of ethanol

*Author to whom correspondence should be addressed. Electronic mail: donglee@pusan.ac.kr. Tel: +82-51-510-2365, Fax: +82-51-512-5236.

(1) Li, C.-L.; Fu, Z.-W. *Electrochim. Acta* **2008**, *53*, 4293–4301.

(2) Lambert, S.; Cellier, C.; Gaigneaux, E. M.; Pirard, J. P.; Heinrichs, B. *Catal. Commun.* **2007**, *8*, 1244–1248.

(3) Liu, Z.; Bando, Y. *Adv. Mater.* **2003**, *15*, 303–305.

(4) Valentini, F.; Biagiotti, V.; Lete, C.; Palleschi, G.; Wang, J. *Sens. Actuators, B* **2007**, *128*, 326–333.

(5) Dhas, N. A.; Raj, C. P.; Gedanken, A. *Chem. Mater.* **1998**, *10*, 1446–1452.

(6) Kim, Y. H.; Lee, D. K.; Cha, H. G.; Kim, C. W.; Kang, Y. C.; Kang, Y. S. *J. Phys. Chem. B* **2006**, *110*, 24923–24928.

(7) Athanassiou, E. K.; Grass, R. N.; Stark, W. J. *Nanotechnology* **2006**, *17*, 1668–1673.

(8) Kang, Y. C.; Park, S. B.; Kang, Y. W. *Nanostruct. Mater.* **1995**, *5*, 777–791.

(9) Hahn, H.; Eastman, J. A.; Siegel, R. W. *Ceram. Trans.* **1988**, *1B*, 1115.

(10) Hahn, H.; Averbeck, R. S. *J. Appl. Phys.* **1990**, *67*, 1113.

(11) Vollath, D.; Sickafus, K. E. *Nanostruct. Mater.* **1992**, *1*, 427.

(12) Lyons, S. W.; Wang, L. M.; Kodas, T. T. *Nanostruct. Mater.* **1992**, *1*, 283.

(13) Kaneko, K.; Moon, W.-J.; Inoke, K.; Horita, Z.; Ohara, S.; Adschiri, T.; Hiroya, A. H.; Naito, M. *Mater. Sci. Eng. A Struct.* **403**, 32–36.

(14) Kawano, M.; Yoshida, H.; Hashino, K.; Ijichi, H.; Suda, S.; Kawahara, K.; Inagaki, T. *J. Power Sources* **2007**, *173*, 45–52.

(15) Michel, C. R.; López, E. R. *Mater. Res. Bull.* **2006**, *41*, 209–216.

(16) Kang, H. S.; Kang, Y. C.; Park, H. D.; Shul, Y. G. *Mater. Lett.* **2003**, *57*, 1288–1294.

(17) Kim, J. H.; Germer, T. A.; Mulholland, G. W.; Ehrman, S. H. *Adv. Mater.* **2002**, *14*(7), 518–521.

(18) Jayanthi, G. V.; Zhang, S. C.; Messing, G. L. *Aerosol Sci. Technol.* **1993**, *19*, 478.

(19) Majumdar, D.; Shefelbine, T. A.; Kodas, T. T. *J. Mater. Res.* **1996**, *11*, 2861–2868.

(20) Kim, J. H.; Babushok, V. I.; Germer, T. A.; Mulholland, G. W.; Ehrman, S. H. *J. Mater. Res.* **2003**, *18*, 1614–1622.

(21) Lee, S. G.; Choi, S. M.; Lee, D. *Thermochim. Acta* **2007**, *455*(1–2), 138–147.

(22) Mahadevan, R.; Lee, D.; Sakurai, H.; Zachariah, M. R. *J. Phys. Chem. A* **2002**, *106*, 11083–11092.

(23) Lee, D.; Park, K.; Zachariah, M. R. *Aerosol Sci. Technol.* **2005**, *39*(2), 162–169.

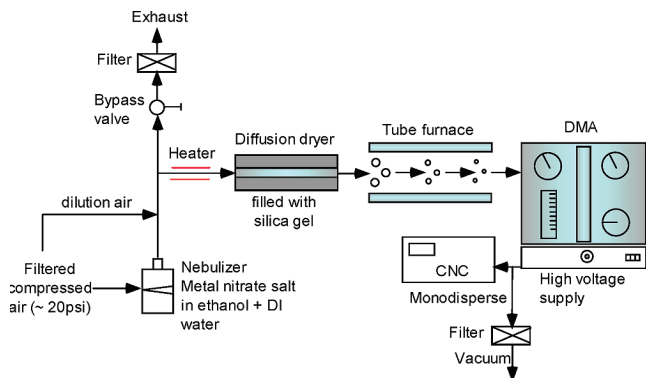


Figure 1. Schematic of experimental setup.

concentrations and temperatures by using X-ray diffraction (XRD). Interestingly, the phase transformation is accompanied by changes in overall morphology and microstructure. A new mechanism responsible for the initiation and progress of the phase reduction is then proposed on the basis of the XRD analysis results, thermodynamic calculation, and high-resolution transmission electron microprobe (HT-TEM) observation. Finally, possible reasons for the morphology change will be discussed.

2. Experimental Section

Cu and/or Cu_2O nanoparticles are generated by spray pyrolysis of copper nitrate (0.1 mol L^{-1} H_2O)–water–ethanol solutions. The copper nitrate salts of reagent grade (99.9% purity) are dissolved in either pure deionized (DI) water or a mixture of DI water and ethanol (99.9% purity) in the range 0–50% volume fraction of ethanol. High-pressure ($2 \times 10^4 \text{ Pa}$) nitrogen gas (99.98% purity) is used to nebulize $\sim 1\text{--}3 \mu\text{m}$ precursor droplets. The nebulized precursor solution aerosols are passed through a stainless steel heat tube at $100 \text{ }^\circ\text{C}$ to partially evaporate the solvent and prevent its recondensing to the tube wall. Droplets are then further dried using a diffusion dryer filled with silica gel and then passed to a tubular furnace with 30 cm long hot zone (Barnstead 21100) with the flow rate of 5 lpm (residence time of 0.27 s). The furnace set temperatures are varied from 450 to $600 \text{ }^\circ\text{C}$ in this study. Inside the furnace, the dried precursor particles decompose to nitrogen oxide gas (NO_x) and copper oxide in the form of Cu_2O or CuO . Further solid-phase reaction might take place to reduce the copper oxide to metallic copper under the reducing atmosphere produced by ethanol decomposition. Product particles are then collected by the electrostatic precipitator for further characterization. Scanning mobility particle sizer (SMPS) consisting of differential mobility analyzer (DMA) and condensational particle counter (CPC, TSI 3010) is also used to analyze particle size distribution. More details of the instrumentation are described elsewhere.^{21–23}

Size, morphology, and elemental composition of the final product particles are characterized with high resolution transmission electron microprobe (HR-TEM, Hitachi H-7600, 200 keV) equipped with energy dispersive spectroscopy (EDS). A 3 mm diameter carbon-coated SiO_2 TEM grid is mounted on top of a deposition substrate of the electrostatic precipitator (ESP) and used to capture the flowing particles for TEM observation. A part of powder samples collected by the ESP is brought to the XRD measurement (D/Max-2400, Rigaku). The XRD pattern of each sample is obtained by scanning the range $35\text{--}53^\circ$ in 2θ unit with $4^\circ/\text{min}$, while irradiating $\text{Cu K}\alpha$ X-ray (30 kV, 40 mA, 0.15405 nm). Each area of the biggest peaks of $\text{Cu}_{(111)}$ and $\text{Cu}_2\text{O}_{(111)}$ at 43.5° and 36.9° , respectively, is analyzed to obtain relative concentrations of each component at different temperatures.

3. Results and Discussion

3.1. Effects of Ethanol on Particle Size, Morphology, and Crystalline Phase.

Figure 2 shows size distributions of

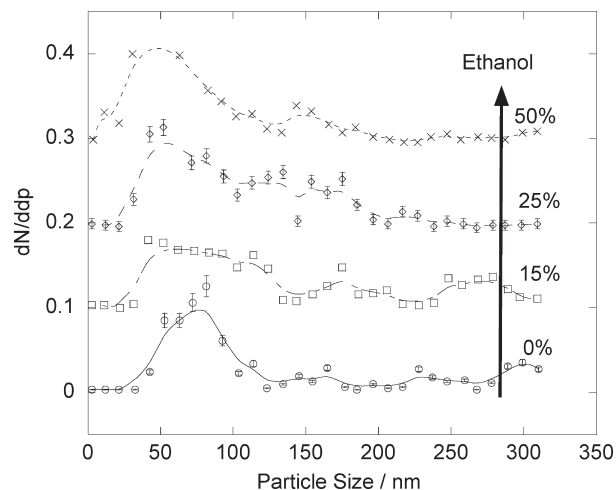


Figure 2. Size distributions of primary particles synthesized with various ethanol contents at $600 \text{ }^\circ\text{C}$.

particles for various volume fractions of ethanol from 0 to 50% in the precursor solution. As the ethanol addition increases, the mode size of particles decreases gradually from 80 to 50 nm. TEM observations indicate that, in the absence of ethanol, the majority of particles have spherical but hollow structures. When ethanol is added, however, solid-like particles appear more often, while the population of the hollow particles decreases. Figure 3 highlights the morphological change when the ethanol content increases from 0% to 15 and 50%. TEM images are analyzed for measurements of shell thickness and diameter of hollow particles. Figure 4a shows how the shell-like particles are distributed in size compared to the total size distribution. In the absence of ethanol, solid-like particles exist only in the size range smaller than 100 nm. Since smaller particles have thinner shell structures as seen in Figure 4b, original shells of some particles smaller than 100 nm are likely to be broken and collapsed, thereby resulting in appearance of solid-like particles.

The size of spray-dried particles is in theory proportional to not only initial size of a parent droplet, but also concentration of the inorganic salt unless the particle is fragmented in the furnace. The maximum temperature used in this study is only $600 \text{ }^\circ\text{C}$, not so high to explode the partially dried droplet into smaller fragments, because the number concentration of particles is almost invariant. Neglected fragmentation, the particle size d_p is proportional to the size of the parent droplet d_d . As solute concentration is not varied throughout this study, mass of solute m_s in a droplet should be proportional to the droplet volume d_d^3 ($m_s \propto d_p^3$). The solid mass in the shell structure is also proportional to the product of surface area and thickness ($m_s \propto d_p^2 \times t$). Therefore, the outer diameter of hollow particle has a linear relationship with the shell thickness ($d_p \propto t$), which is exactly what is observed in Figure 4b.

For a collision-type nebulizer, the addition of ethanol did not change the droplet size distribution. Thus, the differences arising from the addition of ethanol would be chemical in nature and not related to droplet size. Of particular relevance is that copper nitrate is much more soluble in water than in ethanol. Thus, an increase in ethanol content results in the effect of reducing the amount of water, where the salt is going to dissolve, as much as the ethanol is added, and thereby decreasing the absolute amount of salt in a droplet. This partly explains why the dried particles get smaller with increasing ethanol content.

Now, let us address the morphology change. Jayanthi et al.¹⁸ established the first mathematical model to describe spray-drying. When solvent evaporates, the dissolved salt is locally

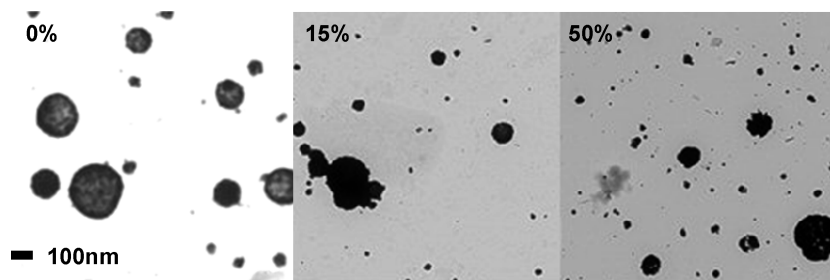


Figure 3. Morphological change from the shell structure to collapsed solid-like particles induced by the addition of ethanol at 600 °C; the ethanol content increased from 0% to 15% and 50%.

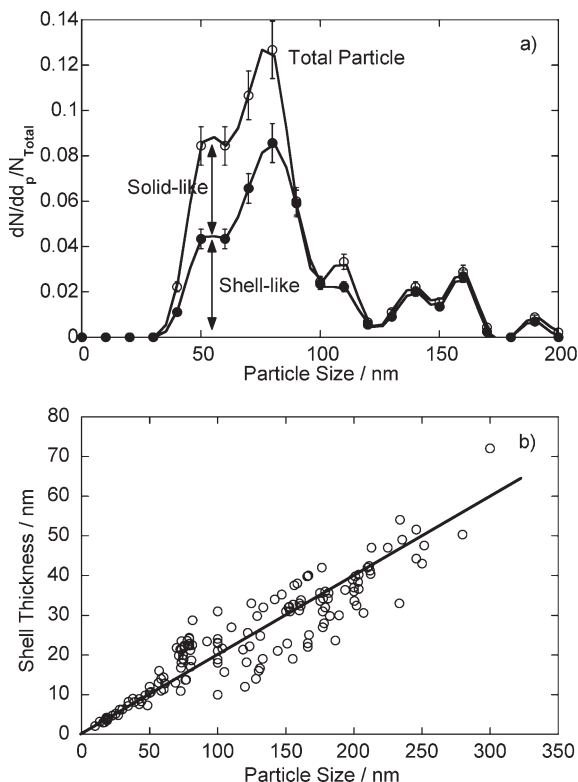


Figure 4. Size-dependent existence of the shell-like particles synthesized in the absence of ethanol at 600 °C: (a) size distributions of shell-like and solid-like particles; (b) dependence of shell thickness on particle size.

concentrated near the droplet surface and diffuses toward the center of the droplet in response to the concentration gradient. As such an increased evaporation rate will lead to a higher salt concentration near the droplet boundary. If the salt concentration approaches the solubility limit, local precipitation at the radial edge of the droplet will result in a hollow particle. Extending their model, Lenggoro et al.²⁵ clarified the influence of operating parameters on the morphology of particles during spray pyrolysis. They concluded that hollow zirconia particles were, in general, formed at faster evaporation conditions, i.e., high reactor temperature, high gas flow rate (short residence time), and low initial solute concentration. It is interesting to note that the model of Jayanthi et al. for spray-drying was successfully applied to predict the morphology of spray-pyrolyzed particles.^{18,26,27}

(24) Willeke, K.; Baron, P. A. *Aerosol Measurement: Principle, Techniques, and Applications*; Van Nostrand Reinhold: New York, 1993.

(25) Okuyama, K.; Lenggoro, I. W. *Chem. Eng. Sci.* **2003**, *58*, 537–547.

(26) Lenggoro, I. W.; Hata, T.; Iskandar, F.; Lunden, M. M.; Okuyama, K. *J. Mater. Res.* **2000**, *15*, 733–743.

(27) Kim, S. H.; Liu, B. Y. H.; Zachariah, M. R. *Chem. Mater.* **2002**, *14*, 2889–2899.

Again, in the absence of ethanol, the existence of hollow particles as seen in Figure 3 implies that the present condition corresponds to fast evaporation. We can consider the morphology evolution as characterized by two characteristic times for solute diffusion and droplet shrinkage induced by solvent evaporation.²⁷ The characteristic time for solute diffusion τ_{sd} is defined as the ratio of surface area (d_d^2) of a droplet to the solute diffusion coefficient (D_s).²⁷ For a dilute solution at 298 K, the D_s can be evaluated as $D_s = [298R_g(1/v^+ + 1/v^-)]/[F^2(1/\lambda_+^0 + 1/\lambda_-^0)]$, where R_g is the gas constant, F is Faraday constant, v^+ and v^- are valences of cation and anion, and λ^0 is the limiting ionic conductance.²⁸ D_s in our 0.1 M $\text{Cu}(\text{NO}_3)_2\text{-H}_2\text{O}$ solution at 298 K is estimated to $1.2 \times 10^{-5} \text{ cm}^2/\text{s}$ by using $\nu^{\text{Cu}^{2+}} = 2$, $\nu^{\text{NO}_3^-} = 1$, $\lambda_{\text{Cu}^{2+}}^0 = 54.0$, and $\lambda_{\text{NO}_3^-}^0 = 71.4 \Omega^{-1} \text{ cm}^2 \text{ mol}^{-1}$. The τ_{sd} is ca. $8.1 \times 10^{-4} \text{ s}$ for a $1 \mu\text{m}$ droplet. The characteristic time for droplet shrinkage is given as $\tau_s = R_g T_p \rho_p d_d^2 / (8 D_v M_v P_{v,\text{sat}}(T_p))$,²⁷ where T_p and ρ_p are temperature and density of the droplet, and M_v and $P_{v,\text{sat}}$ are molecular weight and saturation vapor pressure of water vapor, respectively. Using a diffusion coefficient for water vapor (D_v) of $0.26 \text{ cm}^2/\text{s}$,²⁴ the τ_s is estimated to $\sim 2.1 \times 10^{-4} \text{ s}$, four times shorter than the τ_{sd} . As temperature increases, the τ_s becomes shorter than the τ_{sd} due to strong temperature dependence of $P_{v,\text{sat}}$. This simple comparison supports again that the present experiment was made under the fast evaporation condition.

As 3-fold more volatile ethanol replaces a part of water in the same-sized droplet, the solvent evaporates faster. Also, as aforementioned, ethanol addition reduces initial solute concentration. These all create a favorable condition for the formation of hollow particles. However, the experiment shows the opposite trend such as a hollow-to-solid morphology change. Ethanol–water vapor evaporated from a droplet decomposes to hydrogen and carbon monoxide, which can then reduce the copper oxide to metallic copper, as confirmed by XRD measurements in Figure 5. The phase reduction is possible only when ethanol is added. It is also plausible to think that the morphology change is closely related to the phase reduction. To clarify the idea, we conduct EDS spectroscopy for particles of two different morphologies in the absence of ethanol. Figure 6 shows that shell-like particles contain more oxygen than the solid-like particles. This suggests the possibility that the crystalline phase transition might generate some kind of instability in and collapse the shell structure. We will pursue this conjecture in the subsequent discussions.

3.2. Particle Evolution with Increasing Reaction Temperature. The effect of reaction temperature from 450 to 600 °C at 15 vol % content of ethanol on particle morphology is shown in Figure 7. While particle morphology does not change much until 575 °C, the shell-like particles clearly disappear at 600 °C. Recalling the EDS results, we would expect that particles at

(28) Reid, R. C.; Prausnitz, J. M.; Poling, B. E. *The Properties of Gases and Liquids*, 4th ed.; McGraw-Hill: New York, 1987.

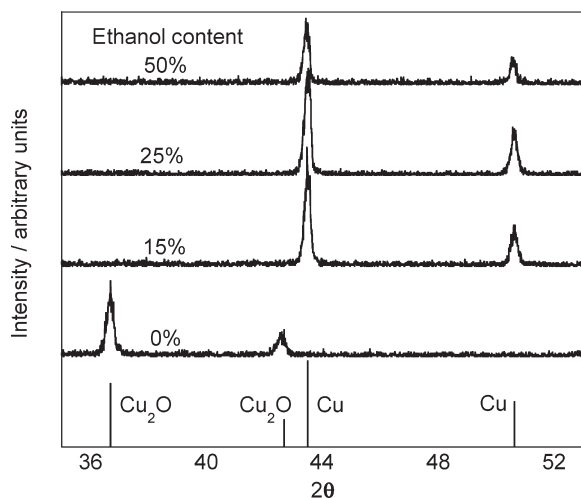
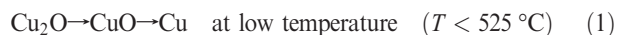


Figure 5. XRD patterns of particles obtained with various ethanol additions at 600 °C.

600 °C contain a very low level of oxygen or are close to metallic copper. XRD profiles corresponding to each temperature show clearly in Figure 8a that initially Cu₂O particles at 450 °C are completely converted to pure metallic copper at 600 °C. Crystalline phase reduction is again accompanied by morphological change, similar to the observation in Figure 3.

Figure 8a indicates that Cu₂O is the sole product of spray pyrolysis of copper nitrate at 450 °C in the presence of ethanol. The biggest peak at 36.9° in 2θ units corresponds to diffraction of Cu₂O₍₁₁₁₎. As temperature increases to 500 °C, new peaks appear at 36.0° and 39.2° corresponding to the diffractions of CuO₍₀₀₂₎ and CuO₍₂₀₀₎, respectively. At 525 °C, a new Cu₍₁₁₁₎ peak is observed at 43.5°, while both intensities of the CuO peaks decrease and then completely disappeared at 550 °C, implying that the newly formed CuO crystallite is reduced to metallic Cu. By 600 °C, Cu₂O peak has disappeared and the Cu₂O-to-Cu phase reduction is complete.

In order to address the observations quantitatively, XRD profiles are analyzed to estimate peak areas of Cu₂O₍₁₁₁₎, CuO₍₀₀₂₎, and Cu₍₁₁₁₎. A mole fraction (X_i) of one of those species can then be approximated by normalizing a peak area with the sum of the three peak areas. Figure 8b shows that, in the low-temperature range 450–525 °C, almost 10% of Cu₂O is first oxidized to CuO, followed by phase reduction of CuO to Cu. Apparently, the Cu₂O seems to be more stable than CuO in the temperature range and thereby not involved in the production of Cu (see no change in Cu₂O in Figure 8b). This implies that CuO has a lower activation barrier for the reduction than Cu₂O does, which is consistent with the finding of Kim et al. from a reduction experiment for commercial powders of CuO and Cu₂O.²⁹ At higher temperature (> 525 °C) where CuO is negligible, Cu₂O undergoes a direct reduction to Cu. These findings suggest that the solid-state crystalline phase reduction in the aerosol state follows two pathways:



Here, we would point out two interesting things. (1) Despite the lack of nominal source of molecular oxygen, some of Cu₂O is oxidized at $T \leq 500$ °C. In the inert gas (N₂) environment, 2 mol

of copper nitrate is spray-pyrolyzed to produce several moles of O₂ as

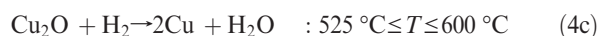


Moreover, the carrier gas N₂ was reported to contain ~200 ppm of oxygen as an impurity from the vendor. Even though the level of oxygen itself coming from copper nitrate is high enough to oxidize the entire Cu₂O, only 10% of Cu₂O was oxidized. This suggests that only a small fraction of the oxygen is available for the Cu₂O oxidation after consuming any reducing agents generated from ethanol decomposition. (2) Why does the Cu₂O not take the easy route for phase reduction (eq 1) at $T \geq 525$ °C? In this temperature range, the reducing agent seems to prevail over the oxygen in the reactor, thereby consuming the oxygen before oxidizing Cu₂O in contrast to the case of 500 °C. This seems to restrict the CuO formation. Thus, the direct path of eq 2 is the only channel for Cu₂O phase reduction at high temperature.

In order to confirm this conjecture, we conducted the following gas-phase compositional analysis for ethanol decomposition. On the basis of SMPS-measured size distribution of Cu₂O particles denoting volume-mean diameter $d_{v,p}$ of 152 nm, total number density N_T , and volume-mean diameter $d_{v,d}$ of parent droplets are calculated to be $3.74 \times 10^6/\text{cc}$ and $1.51 \mu\text{m}$, respectively, and then applied to estimate the mole concentrations of C₂H₅OH and H₂O before the diffusion dryer removing ~86% of the water vapor. Using NASA CEA code, equilibrium calculations are made for ethanol decomposition from the C₂H₅OH–H₂O mixture with the molar ratio of 1:3 as expected after the dryer. Figure 9a shows the resultant composition of gaseous products as a function of temperature. The H₂ is the major reducing agent over all temperatures of interest and the most rapidly evolving species as temperature increases.

The mole fraction of H₂ in Figure 9a when multiplied by the total mole concentration of the binary mixture approximates to the mole concentration of the H₂. In addition, accounting for eq 3a or 3b, the mole concentration of O₂ coming from copper nitrate can be higher or lower estimated directly from that of Cu₂O. As such, Figure 9b compares such mole concentrations of H₂ and O₂ in the unit of ppm. Note that the oxygen level X_{O_2} starts from 200 ppm corresponding to the level of O₂ impurity from the carrier gas and splits into the two limits at 400–425 °C. Also, Figure 9b indicates the level of hydrogen X_{H_2} required for both the oxidation of the O₂ and the reduction of the Cu₂O. Obviously, the selection of the reaction pathways in eqs 1 and 2 is determined by the availability of the H₂ as described before. Hereafter, we would rather focus on the direct reduction of Cu₂O at $525 \text{ } ^\circ\text{C} \leq T \leq 600 \text{ } ^\circ\text{C}$ where the H₂ seems not to be the issue and the phase reduction mainly occurs with morphology change.

3.3. Reaction Kinetics of the Cu₂O Reduction. This section describes investigations of the reaction kinetics and apparent activation energy for Cu₂O reduction. We begin with an explanation of how we estimate the degree of reaction (α) from the mole fraction (X_i) of a solid species in Figure 8b. From the observations in the previous section, we proposed three distinct reactions depending on the reaction temperature:



(29) Kim, J. Y.; Rodriguez, J. A.; Hanson, J. C.; Frenkel, A. I.; Lee, P. L. *J. Am. Chem. Soc.* **2003**, *125*, 10684–10692.

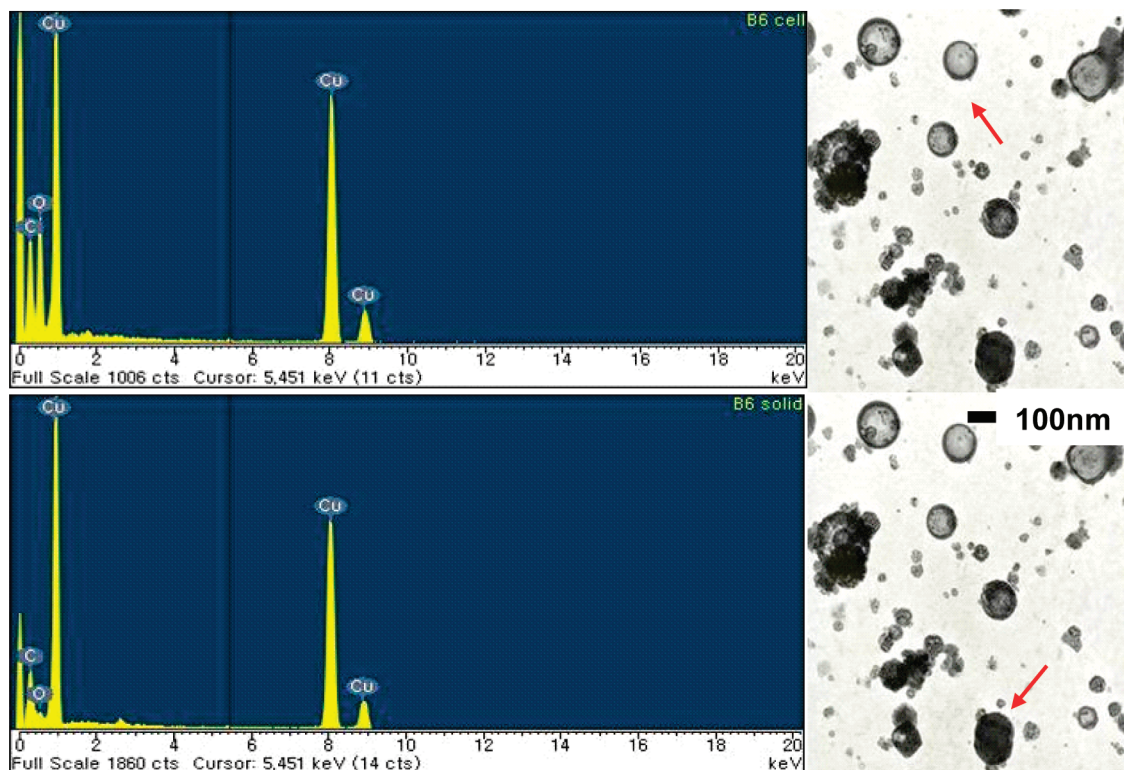


Figure 6. Elemental compositions for a shell-like particle and a solid-like particle. Left spectra measured for a particle indicated by a red arrow.

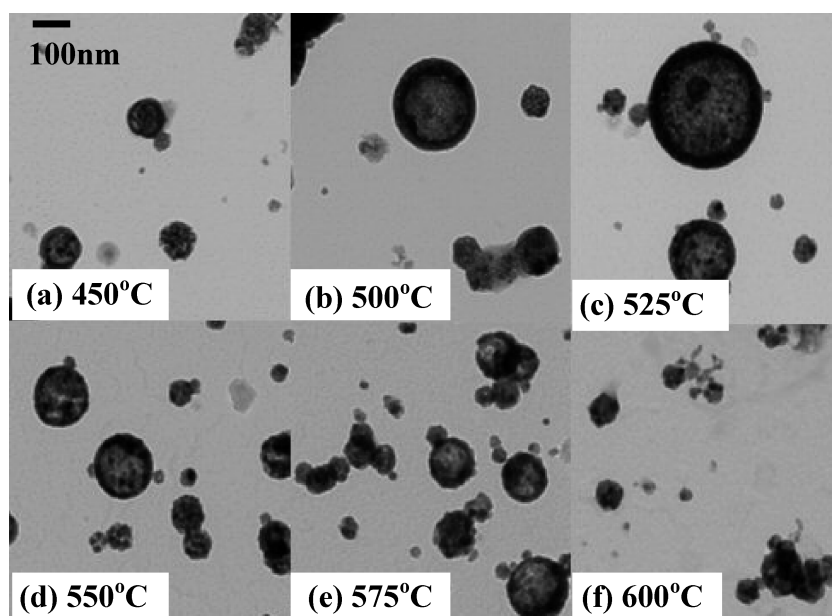


Figure 7. Particle evolution with increasing reaction temperature from 450 to 600 °C.

From eq 4a, β_1 mol of CuO are produced from 1 mol of Cu_2O at 500 °C. At the same time, $(\alpha_1 \equiv 1 - \beta_1/2)$ mol of Cu_2O still remain. Then, a relationship between the β_1 and X_{CuO} is reduced as

$$\beta_1 = X_{\text{CuO}} / (1 - X_{\text{CuO}}/2) \quad (5a)$$

Substituting X_{CuO} from Figure 8b to eq 5a, we found that 1 mol of Cu_2O is turned into 0.149 mol ($=\beta_1$) of CuO plus 0.925 mol ($=\alpha_1$) at 500 °C. As temperature increases over 500 °C, β_1 mol of CuO will react with H_2 through eq 4b and α_1 mol of Cu_2O

will take the route of eq 4c. Additionally, we define α_{CuO} and $\alpha_{\text{Cu}_2\text{O}}$ representing the moles of Cu produced from 1 mol of CuO and Cu_2O , respectively. Hence, at 525 °C, $\beta_1 (1 - \alpha_{\text{CuO}})$ mol of CuO and $\alpha_1 (1 - \alpha_{\text{Cu}_2\text{O}}/2)$ mol of Cu_2O coexist with $(\beta_1 \alpha_{\text{CuO}} + \alpha_1 \alpha_{\text{Cu}_2\text{O}})$ mol of Cu. From the mole fraction of Cu_2O ($X_{\text{Cu}_2\text{O}}$) at each temperature, $\alpha_{\text{Cu}_2\text{O}}$ can be calculated as

$$\alpha_{\text{Cu}_2\text{O}} = \frac{2(1 - X_{\text{Cu}_2\text{O}})\alpha_1 - 2\beta_1 X_{\text{Cu}_2\text{O}}}{(1 + X_{\text{Cu}_2\text{O}})\alpha_1} \quad (5b)$$

As $\alpha_{\text{Cu}_2\text{O}}$ ranges from 0 to 2, a molar degree of Cu_2O reduction (α) in eq 4c is simply $\alpha = \alpha_{\text{Cu}_2\text{O}}/2$.

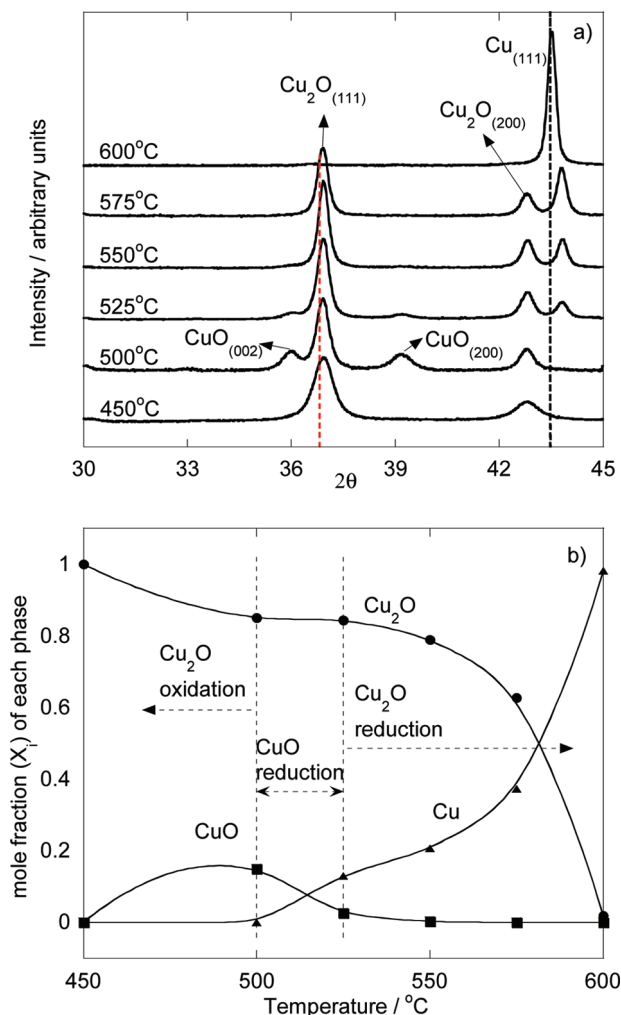


Figure 8. Progress of crystalline phase reduction with increasing temperature in the addition of 15% ethanol. (a) XRD patterns of particles, two dotted lines represent diffraction positions of unstrained lattices; (b) behavior of mole fractions of three species such as Cu, Cu₂O, and CuO as a function of temperature.

It is common for a solid-state reaction rate $d\alpha/dt$ to be expressed as a function of temperature (T) and α :

$$d\alpha/dt = k(T)f(\alpha) \quad (6)$$

where the time t corresponds to the residence time of particles (τ) in the reactor, which is kept constant, $k(T)$ is the rate constant, and $f(\alpha)$ is a mathematical function describing reaction mechanism.^{22,30} The present experiment was done at an isothermal condition for a constant residence time τ . An integral form of eq 6 is more useful for extraction of Arrhenius parameters as follows.

$$g(\alpha) \equiv \int_0^\alpha \frac{1}{f(\alpha)} d\alpha = \int_0^\tau k(T) dt = k(T) \cdot \tau \quad (7)$$

In this study, a nucleation and growth model³⁰ ($g(\alpha) = [-\ln(1 - \alpha)]^{1/3}$) is employed to extract $k(T)$ at different temperatures, where $k(T)$ is assumed to take an Arrhenius form; $k(T) = A \exp(-E_A/RT)$ where A is the pre-exponential factor, E_A is the activation energy, and R is the gas constant. A plot of $\ln(k)$ against $1/T$ in Figure 10 shows the Arrhenius behavior. The activation energy E_A of ca. 141.6 kJ mol⁻¹ is somewhat

(30) Tanaka, H. *Thermochim. Acta* **1995**, *267*, 29–44.

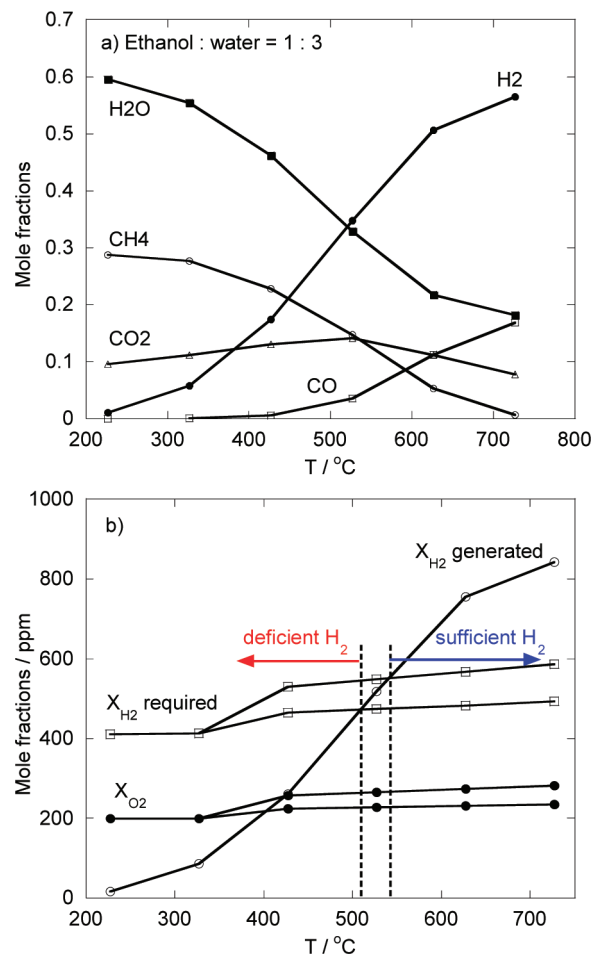


Figure 9. Equilibrium compositional analysis for gaseous products from ethanol decomposition: (a) mole fractions of product gases from 1:3 mixture of ethanol and water vapor, (b) comparison of hydrogen yield with oxygen impurity and Cu₂O aerosols.

higher than the value (114.6 kJ mol⁻¹) reported by Kim et al.²⁹ As characteristics of their commercial Cu₂O powder have not been reported in detail, a direct comparison might be inadequate. When the linear fitting is confined to the range 525–575 °C, however, the E_A shows a better agreement with that of Kim et al., as seen in Figure 10 with a dotted line. Then, the reaction rate constant at 600 °C is likely higher than the value expected by the reaction model. This means there is another factor enhancing the reaction at 600 °C. This might be related to the significant morphology change of particles in the range 575–600 °C, which will be discussed in section 3.5.

3.4. Driving Force for the Phase Reduction. In this section, we develop a thermodynamic analysis to clarify whether the phase reduction is limited by solid-state thermodynamics or not. We begin with the calculation of Gibbs energy difference^{20,31,32} over the reaction of eq 4c. In the presence of an

- (31) Qin, W.; Nagase, T.; Umakoshi, Y. *J. Appl. Phys.* **2007**, *102*, 124303.
 (32) Jeurgens, L. P. H.; Sloof, W. G.; Tichelaar, F. D.; Mittemeijer, E. J. *Phys. Rev. B* **2000**, *62*, 4707.
 (33) Smith, D. L. *Thin-Film Deposition: Principles and Practice*; McGraw-Hill: New York, 1995; Chapter 6.
 (34) Joint Committee on Powder Diffraction Standards - International Centre for Diffraction Data (JCPDS-ICDD) PCPDFWIN software; version 1.30, 1997.
 (35) Girifalco, L. A.; Weizer, V. G. *Phys. Rev. B* **1959**, *114*, 687.
 (36) Pienkos, T.; Gladyszewski, L.; Proszynski, A.; Chocyk, D.; Gladyszewski, G.; Martin, F.; Jaouen, C.; Drouet, M.; Lamongie, B. *Vacuum* **2003**, *70*, 243–248.
 (37) Zhou, G.; Yang, J. C. *Phys. Rev. Lett.* **2004**, *93*, 226101.
 (38) Jiang, Y.; Adams, J. B.; Sun, D. J. *Phys. Chem. B* **2004**, *108*, 12851.
 (39) Vitos, L.; Ruban, A. V.; Skriver, H. L.; Kollar, J. *Surf. Sci.* **1998**, *411*, 186.

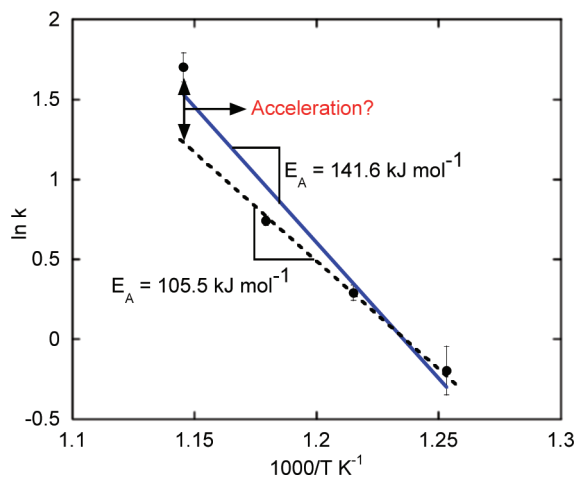


Figure 10. Arrhenius plot for the Cu_2O –Cu phase reduction.

interface between two phases, total Gibbs energy difference (ΔG_T) can be written as a sum of bulk (ΔG_v) and interfacial (ΔG_{int}) terms.³² The bulk Gibbs energy difference for the reaction is given by

$$\Delta G_v = 2G_{v,\text{Cu}} + G_{v,\text{H}_2\text{O}} - (G_{v,\text{Cu}_2\text{O}} + G_{v,\text{H}_2}) \quad (8)$$

where the bulk Gibbs energy G_v of each species is calculated from enthalpy (H_f) and entropy (S_f) of formation as $G_v = H_f - TS_f$, which are obtained as a function of temperature from NIST Chemistry Webbook. If a spherical Cu particle nucleates in a shell region of Cu_2O , the interfacial term arising from Gibbs–Thomson effect is expressed as³¹

$$\Delta G_{\text{int}} = \frac{4\phi N_A V}{d_{c,\text{Cu}}} \quad (9)$$

where ϕ is interfacial tension or energy in the unit of $[\text{kJ m}^{-2}]$, N_A is Avogadro's number, V is mean atomic volume of the two phases, and $d_{c,\text{Cu}}$ is the crystallite size of the Cu phase embedded in the Cu_2O phase, which can be estimated from the XRD profile by the Scherrer equation.

The ϕ value is approximated by the sum of chemical interaction energy ϕ^{int} and strain energy ϕ^{mismatch} as described in detail in the Appendix. Unlike the work of Jeurgens et al.³² where most of the elastic strain was stored in a thin Al_2O_3 layer on top of an Al substrate, we assume that part of Cu_2O and some of Cu from their interface are both strained because Cu_2O is not a minor phase except at 600 °C (see Figure 8b). Thus, the mean values for Cu and Cu_2O are taken for the term of $E/(1 - \nu)$ in eq A3. As 1–5 nm³² or 0.5–2 nm³¹ has been considered for the thickness of the interface (h), the middle value of 2.5 nm is taken in this study. As such, a variety of physical data for the calculation of ϕ are summarized in Table 1.

Applying the lattice spacings and the physical data to eqs A1–A4, we calculate the ϕ as a function of temperature, as summarized in Table 2. The strain of $f \cong 0.15$ due to lattice mismatch at the interface during the phase reduction is significantly larger than that observed in most metal–metal oxide systems ($f = 0.02$ – 0.07).³² For this reason, the ϕ^{mismatch} becomes two times larger than the ϕ^{int} , resulting in positive interfacial energy ϕ greater than free surface tension of Cu or Cu_2O (see Tables 1 and 2). Applying those data in Tables 1 and 2 to eq 9 and using eq 8, we calculate ΔG_v , ΔG_{int} , and ΔG_T at each temperature as summarized in Table 3. Note that, at 600 °C, the ϕ is replaced simply by the surface tension of Cu where no interface exists. The table shows

that ΔG_T is getting more negative with increasing temperature mainly due to decrease in the ΔG_{int} .

Qin et al.³¹ suggested that additional work arising from volume contraction during bcc-to-fcc transition of Fe under compressive pressure could affect phase stability significantly. To evaluate the effect of the work, the pressures built up during the phase reduction are examined as follows. If one considers a hollow Cu_2O particle with outer diameter d_p and shell thickness t_k , the shell region is subjected to a compressive field ($P_{\text{Cu}_2\text{O}}$) induced by doubled surface tension as

$$P_{\text{Cu}_2\text{O}} = \frac{2\sigma_{\text{Cu}_2\text{O}}}{t_k} \cong \frac{2\sigma_{\text{Cu}_2\text{O}}}{0.2d_p} \quad (10)$$

Once a Cu particle nucleates inside the shell, the ϕ drives the Cu nucleus to contract with the assistance of $P_{\text{Cu}_2\text{O}}$, building up a resistant pressure in the Cu particle. The volume contraction will be continued until the driving forces are balanced with the resistant force as

$$P_{\text{Cu}} = \begin{cases} P_{\text{Cu}_2\text{O}} + \frac{4\phi}{d_{c,\text{Cu}}} & \text{at } T \leq 575 \text{ }^\circ\text{C} \\ \frac{4\sigma_{\text{Cu}}}{d_{c,\text{Cu}}} & \text{at } T = 600 \text{ }^\circ\text{C} \end{cases} \quad (11)$$

Noting that the P_{Cu} is the maximum resistant pressure at the time of force balance, we consider two limiting cases: the first one is for no resistance for the volume contraction, maximizing the positive work as $\Delta W_{\text{max}} = P_{\text{Cu}_2\text{O}}(V_{\text{Cu}_2\text{O}} - V_{\text{Cu}})N_A > 0$, and the second one is for the maximum resistance, leading to the negative work as $\Delta W_{\text{min}} = (P_{\text{Cu}_2\text{O}} - P_{\text{Cu}})(V_{\text{Cu}_2\text{O}} - V_{\text{Cu}})N_A < 0$. Here, the work ΔW is approximated by the mean value of the two limiting works. For a hollow Cu_2O particle of 75 nm in outer diameter, the pressures and the work are also listed in Table 3. We find that the adverse contribution of interface ΔG_{int} to the Cu phase stability is partly compensated by the ΔW , so that the effective free energy difference ($\Delta G_T + \Delta W$) gets more negative than ΔG_T alone, indicative of the simultaneous phase reduction with the stronger driving force increasing with temperature.

3.5. Mechanisms for Phase Reduction and Morphology Change. So far, we have discussed on the basis of the assumption that the Cu nucleates in the shell of Cu_2O particle without any justification. Table 2 shows that the Cu lattice is 0.8% compressed with respect to its unstrained lattice at 525–575 °C but suddenly recovered to the unstrained lattice at 600 °C (see the behavior of the lattice spacing $d_{\text{Cu}(111)}$ in Figure 8a). This behavior is exactly consistent with that of P_{Cu} when temperature increases. This is possible only if the Cu crystallites are embedded by Cu_2O matrix below 600 °C. In addition, HR-TEM images were taken near the surface of and inside the shell of Cu_2O at 550 °C. As a result, the Cu nuclei are more often observed inside the shell region rather than at the surface. Figure 11 shows an example of the HR-TEM image taken inside the shell region.

Moreover, though the excess hydrogen exists in the gas phase as seen in Figure 9, solid-state diffusion of H_2 through the Cu_2O shell might be a rate-limiting step of the phase reduction. If this is the case, the Cu should be nucleated at the surface. To rule out this possibility, the characteristic time for H_2 diffusion ($\tau_{\text{D,H}_2} \sim R_p^2/D_{\text{H}_2}$) is calculated for a 100 nm particle ($R_p = 50$ nm) and then compared with the characteristic time for the reaction ($\tau_{\text{react}} \sim 1/k$ in Figure 10). By applying a typical solid-state diffusion coefficient ($\sim 10^{-9}$ cm²/s) to the D_{H_2} , we find the $\tau_{\text{D,H}_2}$ to be $\sim 2.5 \times 10^{-2}$ s, which is at least 1 order of magnitude shorter than the τ_{react} (0.48–1.22 s). Consequently, the H_2 has already been inside the

Table 1. Physical Data for Cu–Cu₂O System at Standard Conditions

name	value	unit
unstrained interplanar distance ³⁴	$d_{\text{Cu},(111)}^0$	2.08×10^{-10}
	$d_{\text{Cu}_2\text{O},(111)}^0$	2.44×10^{-10}
unstrained half-cell dimension for cubic structure	$a_{\text{Cu}}^0 = (h^2 + k^2 + l^2)^{1/2} d_{\text{Cu},(hkl)}^0/2$	1.801×10^{-10}
	$a_{\text{Cu}_2\text{O}}^0 = (H^2 + K^2 + L^2)^{1/2} d_{\text{Cu}_2\text{O},(HKL)}^0/2$	2.113×10^{-10}
atomic volume ³⁵	$V_i = C_i (a_i^0)^3$	
	$C_{\text{Cu}_2\text{O}} = 4$ for bcc structure	
	$C_{\text{Cu}} = 2$ for fcc structure	
	V_{Cu}^0	1.068×10^{-29}
O molar interface area ³²	$V_{\text{Cu}_2\text{O}}^0$	3.774×10^{-29}
	$A_{(O)} = \frac{1}{4} \sqrt{2} (a_{\text{Cu}_2\text{O}}^0)^2 N_A$	9.503×10^3
		$\text{m}^2 \text{mol}^{-1}$
Poisson's ratio ³⁶	ν_{Cu}	0.360
Young's modulus ³⁷	$\nu_{\text{Cu}_2\text{O}}$	0.455
	E_{Cu}	1.240×10^{11}
	$E_{\text{Cu}_2\text{O}}$	3.000×10^{10}
surface tension ^{38,39}	σ_{Cu}	1.9
	$\sigma_{\text{Cu}_2\text{O}}$	0.7

Table 2. Variations of the Interfacial Energy During the Cu₂O-to-Cu Phase Reduction^a

$T/^\circ\text{C}$	$d_{\text{c,Cu}}/\text{nm}$	$d_{\text{Cu},(111)}/\text{\AA}$	$d_{\text{Cu}_2\text{O},(111)}/\text{\AA}$	$\phi^{\text{int}}/\text{kJ m}^{-2}$	f	$\phi^{\text{mismatch}}/\text{kJ m}^{-2}$	$\phi/\text{kJ m}^{-2}$
525	19.8	2.063	2.433	-0.00363	-0.15180	0.00749	0.00386
550	25.4	2.064	2.433	-0.00362	-0.15143	0.00745	0.00383
575	29.3	2.066	2.433	-0.00361	-0.15070	0.00738	0.00376
600	27.7	2.078	-	-	-	-	0.00190

^a $d_{\text{c,Cu}}$ is crystallite size of Cu nuclei, $d_{\text{Cu},(111)}$, and $d_{\text{Cu}_2\text{O},(111)}$ are (111) lattice spacings of Cu and Cu₂O phases, respectively, ϕ represents interfacial tension or energy, and f is the elastic strain induced by the lattice mismatch.

Table 3. Calculations of Gibbs Energy Difference for Phase Reduction as a Function of Temperature^a

$T/^\circ\text{C}$	$\Delta G_{\text{v}}/\text{kJ mol}^{-1}$	$\Delta G_{\text{inf}}/\text{kJ mol}^{-1}$	$\Delta G_{\text{T}}/\text{kJ mol}^{-1}$	$P_{\text{Cu}_2\text{O}}/\text{GPa}$	P_{Cu}/GPa	$\Delta W/\text{kJ mol}^{-1}$	$\Delta G_{\text{T}} + \Delta W/\text{kJ mol}^{-1}$
525	-93.54	11.47	-82.08	0.093	0.874	-5.37	-87.5
550	-94.06	8.85	-85.21	0.093	0.695	-3.98	-89.2
575	-94.57	7.54	-87.02	0.093	0.606	-3.28	-90.3
600	-95.07	1.93 ^b	-93.14 ^b	-	0.275 ^b	-	-93.1 ^b

^a where ΔG_{v} , ΔG_{inf} , and ΔG_{T} represent Gibbs energy differences corresponding to bulk, interface and, total, $P_{\text{Cu}_2\text{O}}$ and P_{Cu} are pressures built in Cu₂O and Cu phases during the phase reduction process, and ΔW is the work done by the pressure which will degrade the driving force for the phase reduction. ^b calculated with free surface tension of Cu.

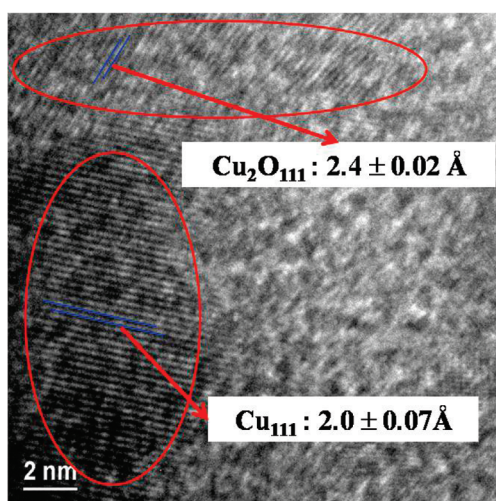


Figure 11. HR-TEM image magnifying an inner region of the shell structure of Cu₂O at 550 °C.

shell region at the beginning of the phase reduction. All these arguments justify the use of the nucleation and growth model in the previous section.

Of particular interest is examination of the size effect of Cu nuclei on the phase stability or the driving force, especially at the beginning of the nucleation. Thus, at 525 °C, the terms of ΔG_{v} , ΔG_{inf} , ΔG_{T} , and ΔW are calculated as a function of Cu nuclei size. As marked with a dotted arrow line in Figure 12, the interfacial term ΔG_{inf} greatly degrades the driving force ΔG_{T} as the size of the Cu nuclei decreases. Note that there is a crossover of the ΔG_{T} line at ~ 2.5 nm below which the positive ΔG_{T} destabilizes the Cu nuclei of such size. However, the critical size is indeed so small as to approach the grain size limit³¹ and even more decreased due to the contribution of ΔW . Thus, the nucleation of Cu seems to happen with a very weak thermodynamic barrier. Once a nucleus forms, it will grow readily to a larger size in order to make the ΔG_{T} more negative. Moreover, regarding the denser structure of Cu compared to that of Cu₂O, higher $P_{\text{Cu}_2\text{O}}$ might be desirable for the nucleation.

Lastly, let us discuss the relationship between the accelerated kinetics in Figure 10 and the morphology change observed at 575–600 °C. As temperature increases near 600 °C, the ΔG_{T} and ΔW become more negative (refer to Table 3) mainly due to the decrease in ϕ and ΔG_{inf} , thereby facilitating nucleation and growth of Cu particles in the Cu₂O shell. If the interface around a growing Cu nucleus approaches the outer surface of the shell, the interfacial tension ϕ likely peels off the thinned part of the outer surface of the Cu₂O. This makes the shell structure greatly

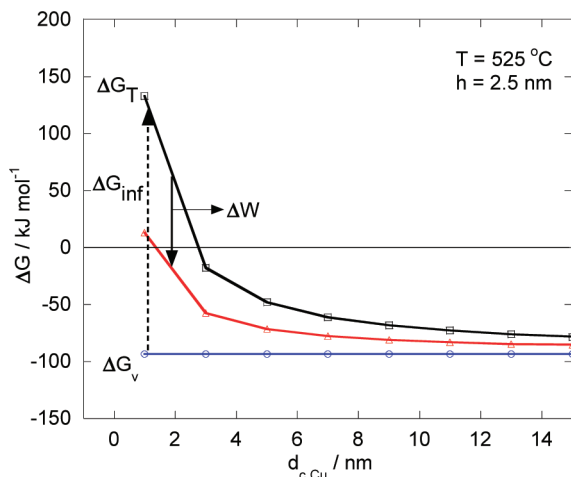


Figure 12. Size effect of Cu nuclei on phase stability.

unstable so that the shell structure begins to collapse. The structural collapse into smaller fragments of Cu_2O suggests that the nucleation of Cu would be enhanced in the fragments of Cu_2O where the greater $P_{\text{Cu}_2\text{O}}$ is expected due to the decrease of its size. This conjecture is consistent with the small decrease in the size of Cu crystallites at 575–600 °C in Table 2 and might be related to the accelerated reduction kinetics.

Overall, we would like to summarize the mechanism for morphology change induced by the phase reduction as follows. Cu nuclei were randomly formed inside of the shell region (refer to Figure 11), which meant that more than one nucleus existed, and then several Cu nuclei grew at different places in a shell region, eventually leading to simultaneous collapse of the shell at several random sites.

4. Conclusions

Copper nanoparticles were produced by spray pyrolysis of copper nitrate with an addition of ethanol as a cosolvent. The current experimental condition in the absence of ethanol was favored to produce shell-like Cu_2O particles. At 15% addition of ethanol to the solvent, all Cu_2O particles were converted to metallic Cu particles, accompanied by a morphological change from a shell structure to solid-like structure. With increasing reaction temperature, initially Cu_2O particles underwent two different reaction regimes: (1) further oxidation to CuO followed by its direct reduction to Cu at low temperature ($450\text{ °C} \leq T \leq 525\text{ °C}$), (2) reduction of Cu_2O to Cu at high temperature ($T \geq 525\text{ °C}$). Gas-phase thermodynamic analysis showed that the first regime was chosen due to the insufficient production of H_2 from the ethanol decomposition at $T \leq 525\text{ °C}$. However, the phase reduction in the second regime was not limited by the H_2 yield, which was confirmed by a simple scaling analysis. The reaction kinetics was also investigated and the resultant activation energy (105.5 kJ mol^{-1}) was in

reasonable agreement with the literature value (114.6 kJ mol^{-1}) below 575 °C. Solid-state thermodynamic analysis suggested that the nucleation and growth model would be the mechanism of phase reduction. We also suggested that the nucleation of Cu happening with a very weak thermodynamic barrier would be enhanced by the structural collapse induced by the interfacial tension.

Acknowledgment. This work was supported by Pusan Clean Coal Center Research Grant.

Appendix. Calculation of interfacial energy

On the basis of the thermodynamic model of Jeurgens et al.³² who described the phase stability of amorphous and γ -phase Al_2O_3 formed on the surface of Al substrate, the interfacial energy ϕ is modeled as a sum of chemical interaction energy ϕ^{int} and strain energy ϕ^{mismatch} induced by a lattice mismatch at the Cu– Cu_2O interface. Though details of the calculations of the terms are available in their work,³² some of equations are introduced briefly for convenience as follows.

The term of ϕ^{int} can be estimated from the enthalpy of mixing ($\Delta H_{\text{O in Cu}}^\infty$) at infinite dilution of 1 mol O atoms in Cu phase as

$$\phi^{\text{int}} = \frac{1}{3} \frac{\Delta H_{\text{O in Cu}}^\infty}{A_{\langle \text{O} \rangle}} \quad (\text{A1})$$

The molar interface area of oxygen $A_{\langle \text{O} \rangle}$ is calculated from the unstrained lattice spacing of Cu_2O and is estimated from the enthalpy of formation $\Delta H_{\langle \text{Cu}_2\text{O} \rangle}^f$ per mole of O by the empirical relation as

$$\Delta H_{\text{O in Cu}}^\infty \cong 1.2 \Delta H_{\text{Cu}_2\text{O}}^f + 1 \times 10^5 \quad [\text{J mol}^{-1} \text{O}] \quad (\text{A2})$$

The term of ϕ^{mismatch} is approximated by the elastic strain energy stored in the interface per unit interface area as

$$\phi^{\text{mismatch}} = h \frac{E}{1-\nu} f^2 \quad (\text{A3})$$

where h is the thickness of the interface storing elastic strain due to the lattice mismatch, E and ν are the Young's modulus and the Poisson's ratio of the interfacial material, respectively, and f is the elastic strain parallel to the interface. The f is approximated by the relative lattice mismatch as

$$f \cong \frac{d_{\text{Cu},(111)} - d_{\text{Cu}_2\text{O},(111)}}{d_{\text{Cu}_2\text{O},(111)}} \quad (\text{A4})$$

where $d_{\text{Cu},(111)}$ and $d_{\text{Cu}_2\text{O},(111)}$ are lattice spacings of the strained lattices that can be calculated from the peak position of each phase by Bragg's diffraction law.